Target delamination by spallation and ejecta dragging: An example from the Ries crater's periphery

Thomas Kenkmann [a],[*], Boris A. Ivanov [b]

[a] Museum of Natural History–Mineralogy, Humboldt-University Berlin, Invalidenstrasse 43, D-10115 Berlin, Germany
[b] Institute for Geodynamics and Geospheres, Russian Academy of Science, Leninsky Prospect, 38, 119334 Moscow, Russia

Abstract

Subhorizontal shear planes (detachments) are observed in bedded limestones in the periphery of the Ries impact crater, Germany. These detachments occur at 0.8–1.8 crater radii distance from the crater center beneath deposits of the continuous ejecta blanket. Striations on detachment planes and offsets of markers indicate top-outward shearing with radial slip vectors. Detachments were found at depths between a few meters and more than 50 m beneath the target surface. The displacements along these faults range from meters to decameters and decrease with increasing depth and distance from the crater center. With increasing crater distance, detachment horizons tend to climb to shallower levels. Cross-cutting relationships to faults associated with the crater collapse indicate that detachment faulting started prior to the collapse but continued during crater modification. Numerical modeling of the cratering process shows that near-surface deformation outside the transient crater is induced by two separate mechanisms: (i) weak spallation by interference of shock and release waves near the target surface and (ii) subsequent dragging by the deposition of the ejecta curtain. Spallation causes an upward and outward directed motion of target material that increases in magnitude toward the target surface. It leads to decoupling of the uppermost target layers in the early cratering stage without totally disintegrating the rock. The subsequent arrival of the oblique impact shower of the ejecta curtain at the target surface delivers a horizontal momentum to the uppermost target area and results in a second horizontal displacement increment by dragging. With increasing depth this effect vanishes rapidly. Spallation decoupling and subsequent ejecta dragging of near-surface rocks is probably a general cratering mechanism around craters in layered targets with weak interbeds.
© 2006 Elsevier B.V. All rights reserved.

Keywords: Ries crater; impact cratering; spallation; ejecta dragging; numerical modeling; detachment

1. Introduction

Impact craters are the most common features on planetary surfaces and result from hypervelocity colli-

sions with asteroids and comets. The near-instantaneous transfer of kinetic energy from projectile to target compresses rocks and causes the generation of a shock wave that expands roughly hemispherically into the target and back into the projectile. Rocks affected by shock are subjected to fracturing, brecciation, shock metamorphism, melting, and vaporization depending on the shock pressure, which in turn depends on the kinetic energy of the impactor and the distance to the point of

* Corresponding author. Tel.: +49 30 20938878; fax: +49 30 2093 8565.
  E-mail address: thomas.kenkmann@rz.hu-berlin.de (T. Kenkmann).

impact. Shock unloading of projectile and target begins when the shock wave is reflected at free surfaces like the rear of the projectile or the target surface surrounding the impact point. Shock and rarefaction waves set target material in motion and initiate an excavation flow that opens the crater at a much lower velocity than the shock wave propagation velocity [1]. The kinematics of the excavation flow are roughly described by the Z-model [2]; the end result is a parabolically shaped crater cavity much larger in size than the diameter of the projectile. The maximum extent of this cavity is known as the transient crater. The end of excavation is reached at the moment when gravity forces stop the outward- and upward-directed motion of non-ejected material at the rim of the crater and reverses its direction to begin the collapse stage of crater formation.

The shockwave front passes through a given point at a specific time, causing the onset of the target material displacement. In the zone of the excavating flow, the main displacement occurs not during the passage of the shockwave, but at a later time during the excavation itself, when the shock wave has expanded far from the excavation zone. However, near to the edge of the excavation zone, outside the transient crater, the stress loading during the passage of the shock front may be more intense than during the following stages of cratering. In this zone displacement of near-surface target, material may manifest itself as decoupling and jumping of coherent plates or blocks without total disintegration of the entire rock. Generally, the target rocks around the growing crater are damaged when applied stresses exceed shear or tensile strength limits. At the periphery of the fragmentation zone, the tensile strength limit is exceeded first, which results in the rock breaking into Grady–Kipp fragments [3,4].

Along free surfaces (zero or ambient pressure planes) surrounding the point of impact, shock waves decay quickly because rarefaction waves rapidly reduce the shock pressure. The volume of material near the surface in which the hemispherically expanding shock wave does not reach its full magnitude due to interference with rarefaction waves is called the interference zone [3]. The thickness of this interference zone depends on the rise time in the shock wave front [1], which is controlled by the target structure (layering, ground water table) and rock properties (e.g., porosity). Target material in this area may be subjected to spallation: Steep pressure gradients accelerate weakly shocked spall plates to specific ejection velocities that may reach a maximum comparable with the impact velocity.

In addition, during the later stages of the crater formation, the uppermost target rocks just outside the transient crater cavity are affected by the deposition of ejecta curtain material. The arrival of the ejecta curtain (end of the excavation phase) postdates spallation (early shock wave propagation) and, thus, encounters a pre-damaged and pre-decoupled target surface which is readily prepared to be partially involved in the outward-directed ejecta-blanket flow. Both processes, near-surface spallation outside the excavated crater and deformation of target rocks during ejecta emplacement, are not yet fully understood. Near the transient crater cavity rim both deformation increments may also be overprinted by the subsequent collapse of the transient crater cavity. The extent of crater collapse depends on impact energy and gravity. The aim of this paper is to detect, analyze, and quantify the effects of weak spallation and ejecta curtain dragging in near-surface target rocks surrounding transient crater cavities. For this purpose we used a combined approach of structural field analysis in the Ries crater and numerical simulations.

The Ries crater (Fig. 1) is the best suited large impact crater on Earth to study processes of excavation and near-surface deformation of target rocks as the amount of erosion is relatively small due to a long period of shielding with post-crater marine sediments [5]. The deposits of the continuous ejecta blanket, the so-called Bunte Breccia, are widely preserved south and east of the crater but were eroded in the north and northwest. They extend up to three crater radii from the crater center. There are numerous sites where the underlying target rocks can be studied at known levels beneath the contact to the ejecta blanket. We have analysed the deformation inventory of parautochthonous and autochthonous target rocks inside and outside the final (structural) crater rim and beneath the Bunte Breccia at distances ranging from 10 to 22 km (0.8–1.8 crater radii) with respect to the crater center. A numerical model of the Ries impact event was used to derive dynamic physical parameters (displacement trajectories, pressure) for the region of interest and to compare these model data with measurements in the field. The combined approach gives clues to the time sequence and deformation processes that lead to the observed structural features.

2. Geological outline of the Ries crater

After Shoemaker and Chao [6] had proven its impact origin, the Ries crater, southern Germany (Fig. 1), became one of the best studied craters on Earth. It is a pristine complex impact crater of ∼26 km diameter that formed during the Miocene. New Ar–Ar laser probe datings of tektites yield an age of 14.34±0.08 Ma [7]. The Ries
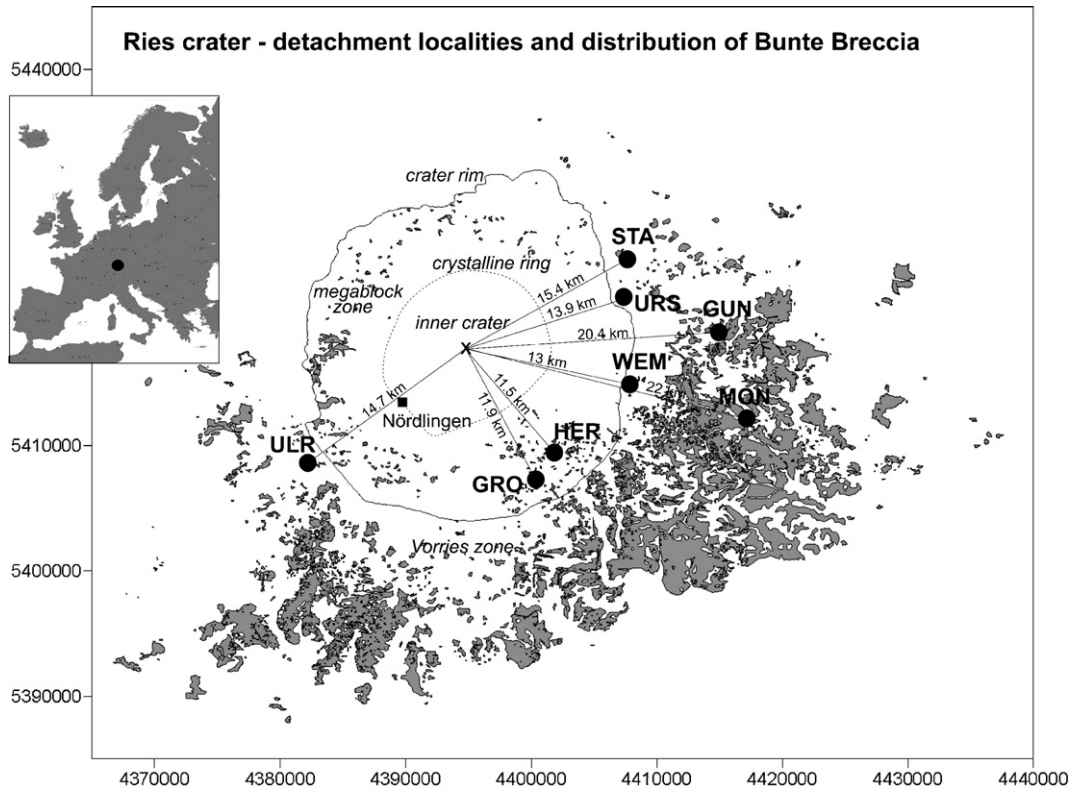
Fig. 1. Simplified map showing the outline of the Ries crater, southern Germany, the distribution of the Bunte Breccia ejecta blanket, and the studied localities that display detachment horizons. Locality abbreviations are explained in the text.

impact occurred in a two-layer target: a 620–750 m pile of well-stratified sediments (limestones, sandstones, shales) of Triassic to Tertiary age and subdued tilting is underlain by crystalline basement rocks (gneisses, granites, amphibolites) [8]. The lowermost part of the sedimentary succession is characterized by sandstone, siltstone while limestones dominate the upper part. Large parts of the Ries surface area were built up of Malmian (Upper Jurassic) limestones when the impact occurred. As a resistant formation these limestones formed an escarpment and displayed a rugged, karstified relief in the southern, western and eastern target area, not unlike to the present-day situation. In the present-day landscape Malmian limestones build up the elevated southern and eastern crater rim but also occur as slumped, parautochthonous blocks as well as ejected megablocks.

The crater consists of an inner crater basin of 12 km diameter that is entirely formed in crystalline basement. The central basin, some 600–700 m deep, has a flat floor and is outlined by a negative residual Bouguer gravity anomaly of −18 mgal [9] and a negative ground magnetic anomaly of −300 mgal which is due to a thick layer of reversely magnetized high-temperature crater

suevite below the lake deposits [10]. The basin is filled with lake deposits of 200–400 m thickness [11]. A structural uplift of 1.5–2 km of crystalline basement underlying the inner basin is recently inferred from reinterpreted geophysical data and numerical simulations [12]. The 1206 m deep Forschungsbohrung Nördlingen 1973 (FBN73) yielded a complete section through the inner crater basin fill and 600 m of the fractured crystalline basement beneath it [13]. Drilling showed that the basin is filled with 300 m of crater suevite that is overlain by 300 m of post-impact lacustrine sediments. The inner crater basin is surrounded by an inner ring formed by crystalline breccias. This crystalline ring forms isolated hills in the present landscape and is believed to roughly coincide with the maximum extent and overturned flap of the transient crater cavity [12]. A shallower annular trough, which is also known as the "megablock zone" is situated between the inner ring and the crater rim (Fig. 1). This megablock zone comprises both allochthonous blocks of brecciated crystalline and sedimentary rocks embedded in Bunte Breccia deposits as well as parautochthonous sedimentary blocks that have slumped into the crater during crater collapse. The hummocky relief of this area is an

expression of its megablock nature. The tectonic crater rim could be defined in several geoelectric traverses [14,15] and a seismic section across the rim [10] by faults that separates autochthonous and downfaulted parautochthonous strata. The area outside the tectonic crater rim, the "Vorries zone", is covered by the continuous ejecta blanket (Bunte Breccia), allochthonous megablocks and patches of suevite. The ejecta of the Ries crater is composed of clastic polymict breccias (Bunte Breccia) that extends up to three crater radii from the impact center as a continuous ejecta blanket of decreasing thickness. Its constituents are mainly sedimentary rocks, with 5–10% of crystalline rocks. The ratio of primary crater ejecta to local substrate components decreases with increasing radial range [16]. Local and crater derived material are thoroughly mixed on all scales. It is interpreted as a "cold", non-cohesive impact formation [16–18]. In contrast, suevitic breccias predominantly consist of variously shocked and partly melted basement material. Recent investigations showed that even the breccia matrix contains high amounts of melted sedimentary and crystalline material [19]. Suevite achieves thicknesses of 300–400 m within the inner crater basin (crater suevite). Outside the crater, it occurs in 10–25-m-thick patches that extend up to two 22 km distance from the crater center (fallout suevite). The suevite-to-Bunte Breccia contact is very sharp and indicates a hiatus and different ejection mechanisms between the emplacement of the Bunte Breccia and the suevite. While the Bunte Breccia deposits are regarded to be formed by ballistic ejection and secondary mass transport [8,16], a process known as ballistic sedimentation [20], the fallout suevite is believed to be settled as a turbulent suspension of melt lumps and solid particles in a medium of hot gases from an expanding vapor plume (e.g., [8,18]). Osinski [21] proposed that the fallout suevite was emplaced as ground hugging impact melt flows. However, an undisturbed suevite-to-Bunte Breccia contact and delicate aerodynamical melt lump features within the suevite argue against this interpretation.

Sharp contacts of the Bunte Breccia ejecta blanket also occur to the underlying rocks [16]. Striations on contact surfaces revealed a radial flow [22,23]. However, obstacles of the pre-existing paleorelief caused deflections by up to 30°. None of the contact planes of the limestone target to the Bunte Breccia represents the ancient pre-impact land surface, since weathering horizons are lacking. Soils and near-surface rocks were incorporated in the ejecta flow. Seidl [24] and Wagner [22] were the first who observed subhorizontal displacements within Malmian target rocks beneath the ejecta blanket-to-target contact and correctly interpreted there

kinematic history. Hüttner [25] and Chao [26] misinterpreted these faults as striated target surfaces.

According to Stöffler et al. [27], the projectile most likely was a binary asteroid that near-simultaneously formed the much smaller Steinheim crater (3.8 km diameter) ~40 km WSW of the Ries crater. Recent modeling [27] suggests an oblique impact from WSW that also accounts for the formation of the fan-like tektite strewnfield (moldavites) in 250–400 km downrange direction in the Czech Republic, East Germany and Lower Austria. The oblique impact scenario, however, did not account for the occurrence of so-called Reuter'sche Blöcke south and southwest of the crater, which are believed to represent spallation products.

3. Methods

3.1. Structural analysis

Slip vectors on shear planes were determined by measuring the orientation of fault striae and grooves. Alternatively, striking of drag fold axes that are associated with the deformation increments of interest were used for flow direction reconstructions. The hinge line of such folds is oriented perpendicular to the slip vector and the fold vergency indicates the sense of shear. Other useful shear sense criteria included the offsets of markers and the ramp-and-flat geometry of detachment planes. The displacement magnitude along a detachment was most simply determined by measuring the offset of a marker parallel to the shear direction. Very useful markers were widened cleavage planes and, in particular, vertically exposed karst pipes and caverns which are frequent in thickly bedded limestones (Malmian δ). Other techniques use the displacement between two benchmarks of the hanging wall and footwall of a fault that initially belonged together. The length of a thrust ramp yields minimum displacement magnitudes. If the hanging wall is folded the minimum displacement can be estimated by calculating the difference between the length of a bed in the fold and the shortest distance from limb to limb. Note that these latter techniques only yield minimum displacement magnitudes. The "true" displacement is not specified and could be orders of magnitude higher.

3.2. Numerical modeling

A two-dimensional numerical model was designed to study the timing and extent of near-surface motion in target rocks surrounding a transient crater cavity. We used the SALEB hydrocode and ANEOS equation of

state for limestone (the upper 800 m) and granite for modeling the Ries target. The computational cell size was mostly 50×50 m (early time control modeling uses 25×25 m cells). We modeled an elliptical projectile equal in volume to a sphere with diameter D of 1.4 km and density 2600 kg/m^3. The use of an elliptical projectile in a two-dimensional model yields a shallower but broader crater cavity than is the case for a spherical projectile, and thus provides a better approximation of the transient crater geometry observed in oblique impact simulations. The chosen impact velocity of 10 km/s corresponds to the vertical component of a 45° oblique impact at 14.1 km/s. The model is computed as an Eulerian grid. To reveal Lagrangian particle motion and display displacements and deformation, tracer mass-less particles (simply named *tracers*), are emplaced in the center of each cell, recording position, pressure and inelastic strain in the target. The cell centered parameters are recalculated for the current tracer position with a bilinear interpolation method. A detailed stress–strain history has been recorded for selected tracers originally placed at ∼13 km distance from the center at various depths. This distance was chosen since most of the structural data were gained from here. Additional tracers cover a radial range from 10 km to 20 km at shallow depth.

A set of additional model parameters was varied to find a best fit to the Ries crater morphology. The parameter study includes a variation in the decay time of acoustic fluidization (25, 20, 16 s), and a change of the friction coefficient in damaged target material (0.4, 0.5) (for model details see, e.g., [28]). The resulting best fit crater has a diameter of 20–22 km and an inner ring of uplifted granite of 12 km diameter that matches the "inner crystalline ring" of the Ries. Note that final crater size and the megablock zone are not reproduced perfectly. Our modeling yields similar results to that of [12].

Due to its two-dimensional axial symmetry the model does not reproduce natural azimuthal variations of target motions as observed in the field, particularly for oblique craters. Moreover, the model at the available resolution describes deformed rocks as a continuum media with a smooth distribution of strain. In contrast, real rocks are predominantly deformed along faults and fractures, separating much less deformed blocks. It is the highly localized strain that is measured in rocks within and around the Ries crater. To correlate field and model data one can estimate the average shear strain, dividing the displacement along a localized shear zone by the characteristic block size. In our case, the effective block size was estimated as a thickness of a detached and displaced upper rock layer. This value can be compared with average shear strain in the model material. To outline the differential motion at the cell size scale

(50 m) we calculated the effective shear strain which is defined as: $s = (x(i,j) - x(i,j-1))/Dy$, where i and j are the indices of cell row and column, respectively, and Dy is the initial cell size.

4. Results

4.1. Structural data

Detachments were exclusively observed in flat-lying limestones of Malmian age, which built up large parts of the Ries target surface at the time of impact. These rocks formed an escarpment and displayed a rugged, karstified relief in the southern, western and eastern target area. With the exception of isolated buttes, these limestones were eroded in the northern part prior to impact. The contact of target surface rocks to the overlying ejecta deposits (Bunte Breccia) is exposed at several sites. Detachments are formed within those limestones that display a rheological stratification formed by interbedded strata of thick limestone beds and thin marly interbeds. Shear zones are always localized in the incompetent layers. Massive reef limestones that occur at the southern rim of the Ries do not show indications of surface-parallel detachment faulting. Figs. 2–4 and the following section describe the individual detachments and the associated deformation inventory of the studied localities. Fig. 5 gives an overview of the structural data and correlates magnitude of displacement, depth of detachment, and distance to the crater center. The following brief description of the outcrops is ordered clockwise with respect to their geographic positions (Figs. 1–4).

4.2. Description of studied localities

Stahlmühle (STA, 15.4 km NE of crater center (cc); 1.23 crater radii): A major detachment plane is exposed in the NE edge of the limestone quarry (out of operation). The length of detachment exposure is ∼40 m in thin-bedded limestones of Malmian *β*. The hanging-wall block shows strata undulations, low-angle strata cut-offs at the detachment, and remarkable folds (Fig. 2c). NW-striking folds display fold planes with NE vergency indicating top-NE motion. One major fold is disharmonic and shows sub-folds in its overturned NE limb (Fig. 2c). The major fold has an amplitude of ∼7 m and is interpreted as a drag fold. A gradational succession exists from detached and dragged blocks (para-utochthonous) to fully isolated megablocks outside the quarry being fully incorporated into the ejecta blanket. Previous outcrop analysis by [25], describing a different outcrop situation, also report thrust planes in Malmian *δ*
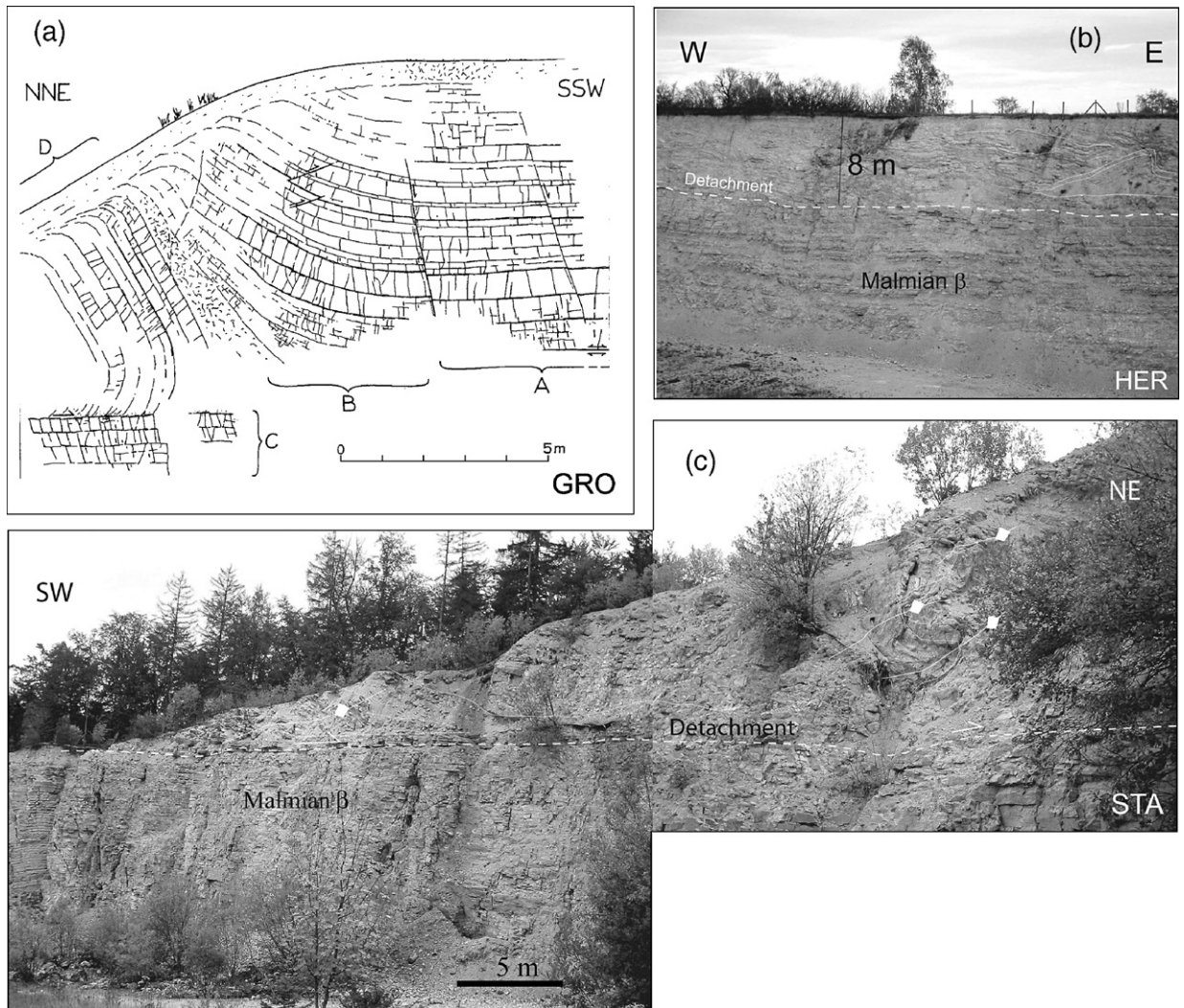
Fig. 2. (a) Grosssorheim (GRO): Line drawing of [22] shows a detachment horizon above unit C in Malmian β limestone. Unit D is locally overturned by drag folding along the detachment. Comminuted and brecciated rock is injected between unit D and A, B. (b) Outcrop situation at Heroldingen (HER) displaying gentle small-scale folding in the hanging wall of a detachment formed in thin-bedded Malmian β limestones. Note that the quarry wall is in an obtuse angle to the tectonic transport direction. (c) Stahlmühle (STA): Asymmetric, disharmonic folding with local overturning occurs in the hanging-wall strata of a Malmian β detachment. Bunte Breccia is situated above the quarry wall.

limestones, and striated contact surface (50–65° strike) to the Bunte Breccia.

Ursheim E (URS, 13.9 km NE of cc; 1.11 crater radii): The flat lying sequence of Malmian β_2 and γ_1 limestones appears rather undeformed, but two bedding-parallel weathered horizons 12–15 m beneath the contact to the Bunte Breccia still exist that show top-E offsets with 1.0–1.2 m displacement of major cleavage planes. Shear planes coincide with interfaces of limestone beds. They were already described by [22] (Fig. 3a) who reports EW striae on these surfaces (90–100° strike).

Wemding (WEM, 12.9–13.4 km E of cc; 1.03–1.07 crater radii): This operating quarry is located at the eastern rim of the crater. The western part displays weakly inclined (10–20° towards NW), thickly bedded limestones of Malmian δ that are partly affected by karstification and that are overlain by remnants of the ejecta blanket. Karst caverns are filled with fluviatile conglomerates (Fig. 4c) of pre-Ries age. Bedding parallel detachment horizons can be observed at different levels between 15 and 30 m depth beneath the contact to the Bunte Breccia (Fig. 4a, b, e) and were also recorded in previous mining stages [14,26]. Top-E
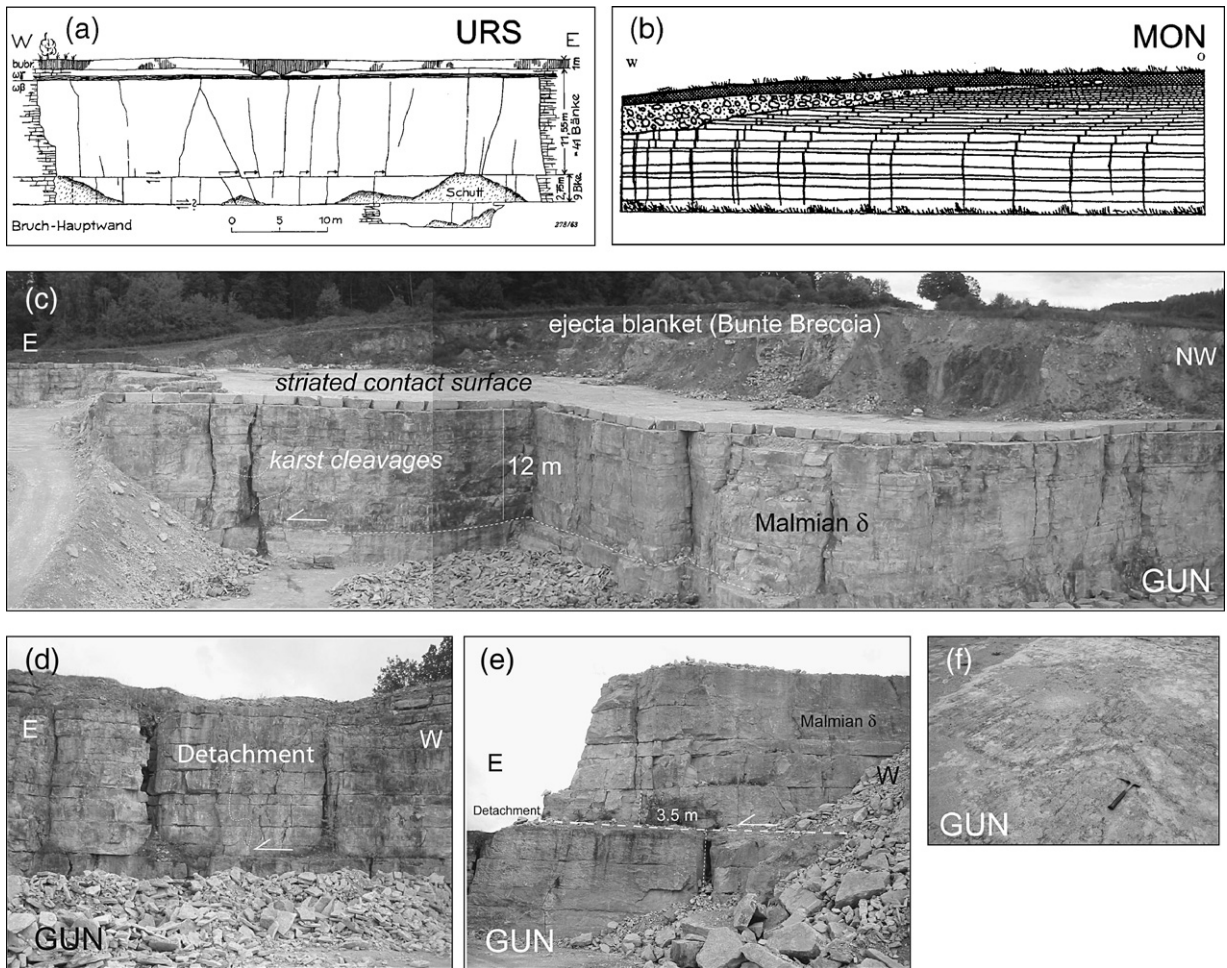
Fig. 3. (a) Ursheim E (URS): Line drawing [22] of plane detachment horizon in flat-lying limestones. The two detachment horizons are localized along thin marly interbeds. (b) Line drawing by [24] illustrating near-surface shearing at Monheim (MON). (c) Main exposure of Bunte Breccia above flat-lying Malmian δ limestones at Gundelsheim (GUN). The detachment occurs 12 m beneath the striated contact surface with visible offset in the E part. (d and e) Close-up of the major detachment at GUN at different exposures. Note the offset of Karst cleavages along the detachment horizon. (f) Contact surface ("Schlifffläche") between Bunte Breccia and target with striae striking 85°.

shearing with displacements ranging from a few meters to probably ≫ 10 m can be inferred from (i) offset of major cleavage planes and vertical karst pipes (Fig. 4b), (ii) low-angle structural cut-offs of strata in the hanging wall of the detachment, and (iii) ramp-and-flat geometries of detachment planes (Fig. 4a). The eastern part of the quarry comprises older, thinner bedded limestones of Malmian α–γ age that are deformed and inclined to variable degrees. A large ~NS-striking and E-dipping reverse fault system separates the western and eastern part (Fig. 4e, f). The vertical throw along this major reverse fault decreases from ~ 60 m in the N to 10 m in the S of the quarry. The reverse shear sense of this fault (top-toward-W) is documented by drag effects and shear sense criteria on the faults (striations, Riedel shear planes) (Fig. 4e, f). Clays and rounded boulders locally lubricate the fault. This material does not represent Bunte Breccia as proposed by [14] but originates from the Karst infill of the pre-Ries age. Based on a more limited exposure, this steeply inclined fault was misleadingly interpreted as a striated paleosurface [14,26] separating parautochthonous rocks (Malmian δ, western part of the quarry) from an allochthonous ejected block (Malmian α–γ eastern quarry). The major reverse fault of the quarry can be genetically linked to deformation increments associated with crater collapse because (i) fault strike is concentric, (ii) movements are radially inward, (iii) the fault has a limited extent and strong variations in offset, and (iv) single-slip displacements are on the order of several meters (see below).
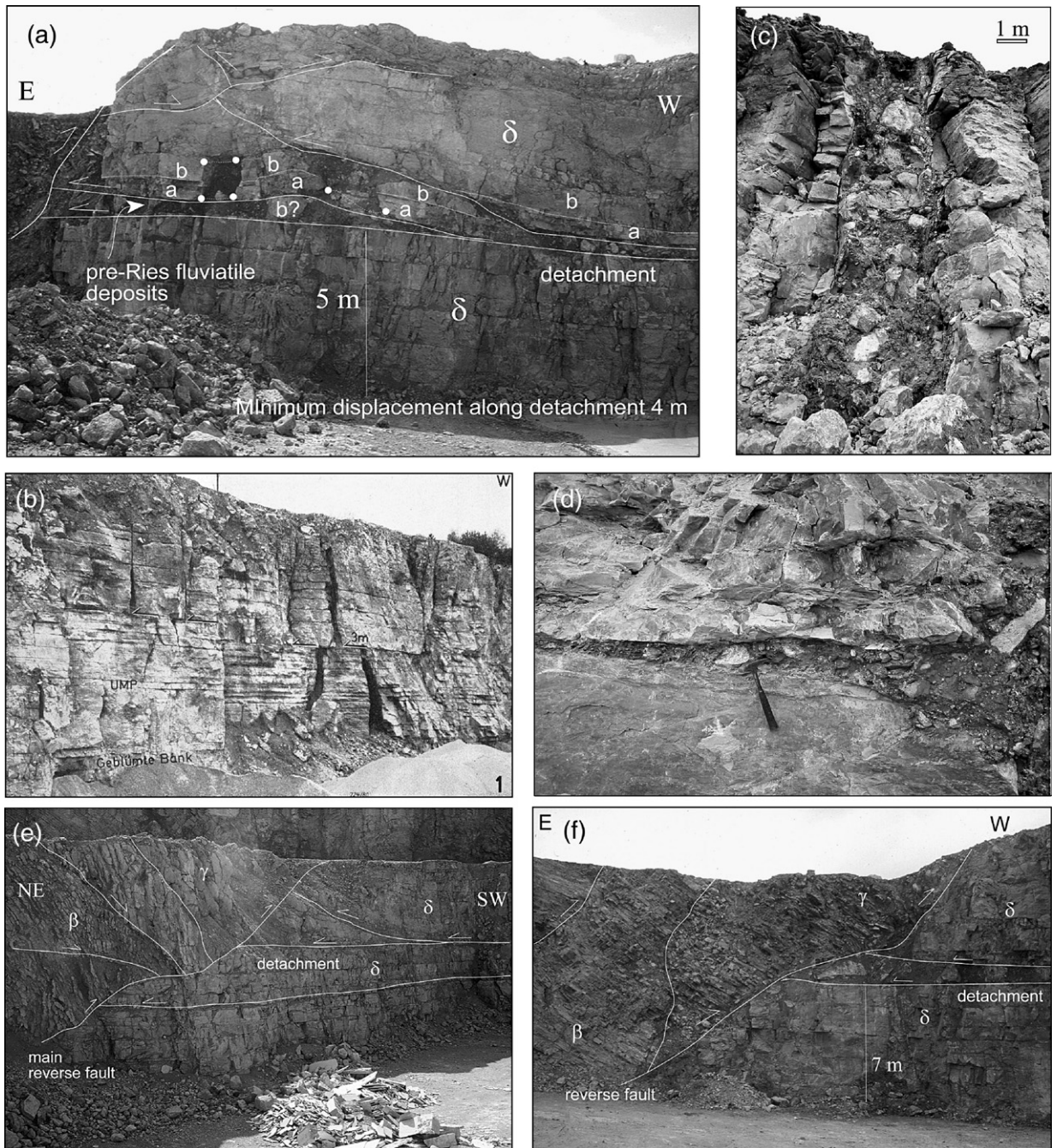
Fig. 4. Wemding (WEM): (a) Detachment and associated hanging-wall deformation in Malmian δ limestone. The detachment is truncated in the E by a reverse fault that was active during crater collapse. Motion on detachment plane is deflected to higher stratigraphic levels. (b) Two main detachment horizons with visible offsets, shown during earlier quarrying operation [23]. (c) Preimpact fluviatile infill of a vertical karst cavern in Malmian δ limestones. (d) Injection of preimpact fluviatile karst pipe infill along a detachment plane. (e and f) Reverve fault associated with crater modification cuts the detachment plane and, therefore, postdates detachment faulting. However, interference of subsidiary faults suggests ongoing radial outward motion.

The detachments of the western unit (Malmian δ) are truncated by the major NS trending reverse fault, and hence, these detachments were formed prior to the reverse fault. Dragging along the main reverse fault caused the opening of the detachment plane (Fig. 4a). This led to an injection of pre-Ries conglomerates and
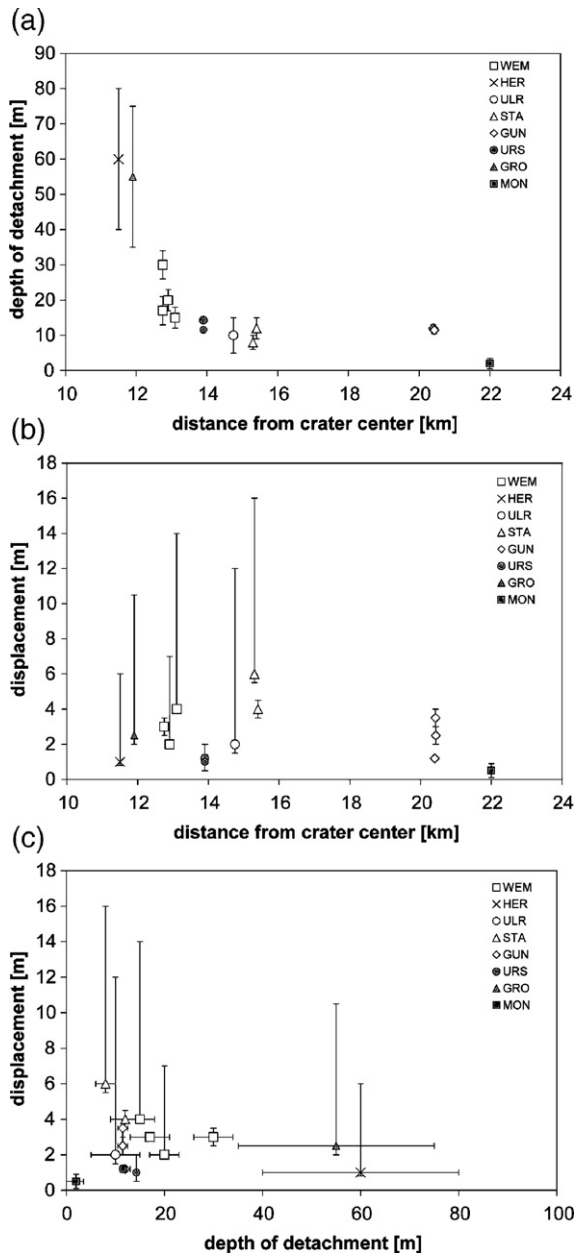
Fig. 5. Summary of structural data of analyzed detachment planes. (a) Distance from crater center versus depth of detachment beneath contact to the Bunte Breccia. (b) distance from crater center versus displacement. (c) depth of detachment versus displacement. For discussion see text.

clays of the Karst pipes (Fig. 4c) into the gaping plane (Fig. 4d). Near the reverse fault, the hanging wall of the detachment shows frequent splays that propagate to higher levels (Fig. 4a). The complex interplay of eastward motion along the detachments and W-directed steep reverse faulting (Fig. 4a, c) indicates that detachment faulting started prior to reverse faulting but was

still ongoing when main reverse faulting occurred. When crater outward motion along the detachment started to be blocked by the onset of reverse faulting, shear planes were deflected to higher stratigraphic levels.

Gundelsheim (GUN, 20.4 km E of cc; 1.63 crater radii): The operating quarry is situated 7.5 km outside the crater rim and displays flat-lying, thickly bedded Malmian δ limestones that are overlain by 8 m of Bunte Breccia (Fig. 3c), composed of limestone and coloured shale blocks. The striated contact surface ("Schlifffläche") with parallel striae and grooves (85° strike) indicates the radial outward directed flow of the Bunte Breccia (Fig. 3f). About 12 m beneath the contact surface a major detachment plane is exposed (Fig. 3c–e) with displacements ranging from 1.2 to 3.5 m. The detachment is localized along a marly interbed and leads to offsets of major cleavage planes and Karst pipes.

Monheim (MON, 22 km E of cc; 1.76 crater radii): An ancient, now non-existent outcrop is described by [24] that illustrates near-surface shearing (Fig. 3b) along several shear planes with displacements in the order of 1 m.

Heroldingen (HER, 11.5 km SE of cc; 0.92 crater radii): Interbedded strata of marls and limestones of Malmian β display small-scaled open folds in the hanging wall of layer-parallel shear planes (Fig. 2b). Small-scale ramp-and-flat thrusts can also be observed and indicate relatively small displacements. The entire sequence was downfaulted during crater collapse. At the southern crater rim Malmian β was overlain by Malmian γ and δ rocks. This must be considered when estimating the depth of detachment.

Grosssorheim E (11.9 km SE of cc; 0.95 crater radii): This old quarry of Malmian β limestones was analyzed in detail by [22]. It shows an upper unit that is decoupled from a basal unit along a flat lying shear plane that is comminuted and striated (135° strike). The upper unit is partly folded. Drag folding leads to local overturning near the detachment (fold strike ~100°) (Fig. 2a).

Ulrichsruhe (ULR, 14.7 km SW of cc; 1.18 crater radii): This quarry outside the crater rim operates in Malmian ζ limestone and dolostone that are overlain by Bunte Breccia. Deformation near the contact to the Bunte Breccia is indicated by thrust planes with ramp-and-flat geometry and associated thrust propagation folds.

4.3. Summary of structural observations and measurements

Detachment faulting along the crater rim and in the periphery of the crater (Vorries zone) always shows
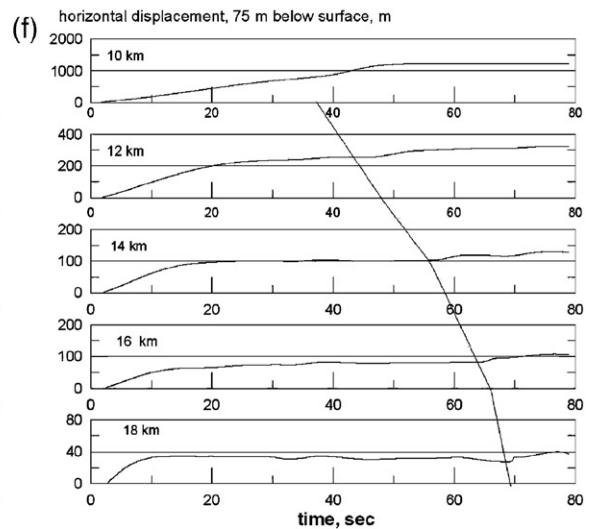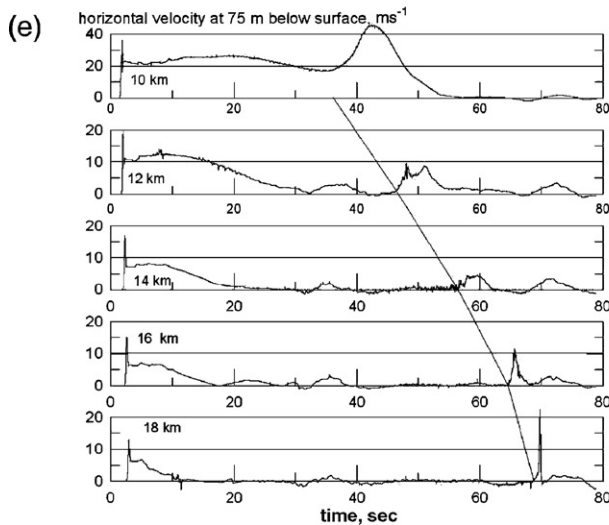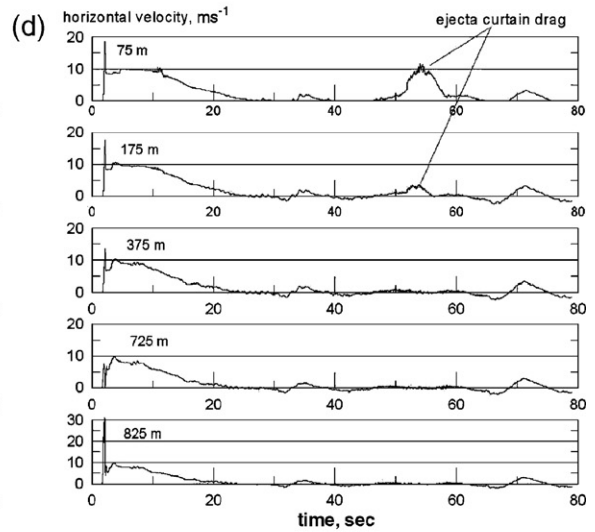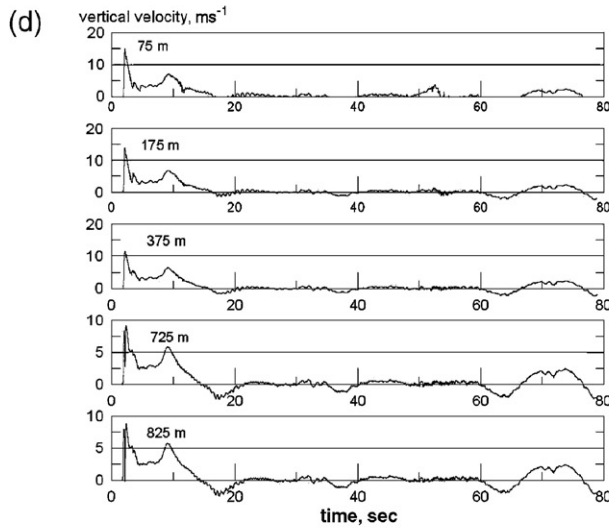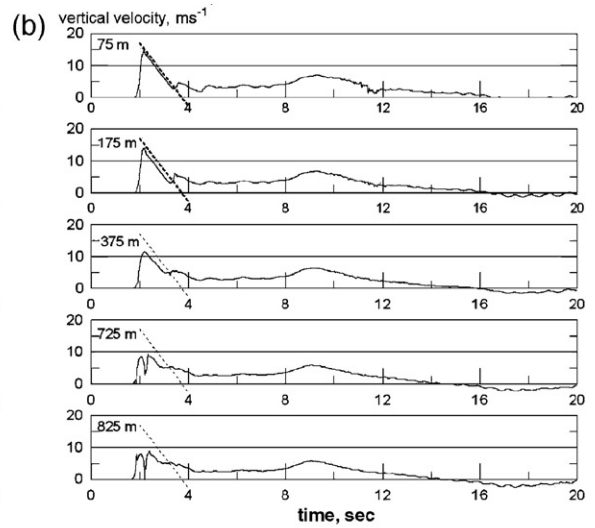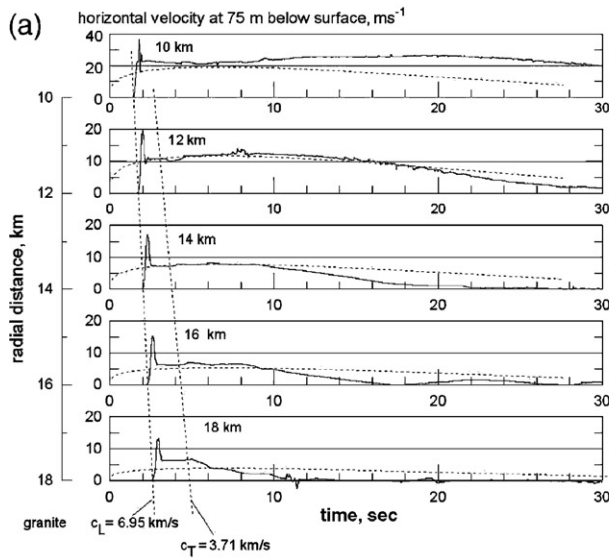
radial top-outward-displacement of the hanging wall block. This is indicated by striations on shear planes, offsets of major cleavage planes and pre-impact karst caverns, and by the vergency of drag folds of the hanging wall strata. Locally a switch in the detachment horizon was observed in the form of ramp-and-flat geometries leading to low-angle cut-offs of strata. Detachments were also recognized by the occurrence of brecciated material injected along the shear planes. Detachments are formed some 1–60 m below the contact of the Malmian to the overlying Bunte Breccia (Fig. 5). The depths of detachment beneath the ejecta blanket decreases with increasing distance from the crater center [29] (Fig. 5a). The measured radial displacement is in the range of 1–15 m. Note that some techniques merely provide an estimate of minimum displacement and produce large error bars in Fig. 5. The magnitude of displacement seems to decrease with increasing distance from the crater center (Fig. 5b), although this trend is not clear. Moreover, the magnitude of displacement seems to increase the shallower the detachment is situated. This suggests a genetic link between the emplacement of the ejecta blanket and the occurrences of detachment planes. The interference of detachments with normal and reverse faults that are linked to the collapse stage of cratering suggests that detachment formation started prior to the crater collapse but had not come to rest when collapse induced faulting started. The structural observations and time relationships reveal that detachment faulting and decoupling of upper target layers started very early and could be caused by moderate to weak spallation outside the transient cavity. Ongoing outward shearing during crater collapse (see WEM) could be related to dragging effects induced by the ejecta curtain [29].

4.4. Results of the numerical simulation

The numerical model derives a sequence of motion events of near-surface target material for double-layer targets that scale to the Ries impact crater (Fig. 6). At the "real" Ries crater, however, the wave motion is expected to be more complex due to multiple reflections and refractions at strata boundaries within its sedimentary succession. Tracer particles recorded the absolute motion of material in the periphery of the transient crater cavity at a depth ranging from 75 m down to 825 m beneath the target surface for a period of 80 s after the impact. The onset of near-surface particle motion (horizontal and vertical) with radial range and depth is displayed in Fig. 6a and b, respectively. The first motion occurs about 2 s after the impact and corresponds to the arrival of stress waves propagating through the basement and refracted to the sedimentary layer (Fig. 6a, b). The rapid decay of this first velocity pulse is due to target fracturing. Subsequent motions in the following 20–30 s is explained with mass motions around the growing transient cavity. For comparison, we calculated the transient cavity growth using the Z-model [2] with $Z = 2.7$ and computed the motion (dashed line) with radial distance. The growth of the cavity lasts about 30 s, followed by the transient cavity collapse. The velocity magnitude for the Z-model and the numerical model is similar, particularly at 12 km distance.

Fig. 6b shows the onset in vertical velocity as a function of time and depth at 13 km radial distance. The profile is indicative to delineate the depth to which spallation occurs. Spallation means the ballistic ejection of decoupled, coherent target blocks. The dashed lines correspond to the free fall in the gravity field. One can see that tracers at initial depths of 75 and 175 m follow this line for 2 s and, thus, experience spallation, whereas tracers at deeper levels (initial depth of 375 m and below) demonstrate the absence of free fall and, hence, the cease of spallation. We introduce the term "weak spallation" to express the low speed and small amount of decoupling.

The entire vertical and horizontal velocity history for the same tracer column is given in Fig. 6c and d. A second horizontal velocity excursion occurs ∼51 s after the impact. This event has only a subdued vertical component. This part of the particle motion can be correlated to the passage of the ejecta curtain (Fig. 7). The horizontal velocity component of the obliquely impacting ejecta reaches a magnitude of 240 m/s near the target surface at 13 km distance from the crater center (Fig. 7). Due to

Fig. 6. Results of the numerical modeling. The horizontal (a, d–f) and vertical (b–c) velocity components of tracer particles are displayed as a function of time. (a) and (b) focus on the early tracer motions, (c–f) display the complete record for 80 s. (a) The shift in the onset of horizontal tracer motion with depth at 13 km distance from the crater center corresponds to the elastic longitudinal sound velocity ($c_L = 6.95$ km/s) for the modeled granitic basement (steep dashed line). Dashed curves in each frame show Z-model predictions for the near-surface ground motion due to transient cavity growth in an incompressible media. (b) Vertical velocity at various depth at radial distance of 13 km from the center. Dashed lines correspond to the free fall in the gravity field. Tracers at initial depth of 375 m and below demonstrate the absence of free fall and, therefore, the cease of spallation. Tracer at 825 m depth is located in the basement. (c, d) Complete history of the vertical (c) and horizontal (d) velocity component of tracers located at 13 km radial distance. Tracers at depths of 75 m and 175 m demonstrate a horizontal motion induced by the passage of the eject curtain drag after ∼51 s. (e, f) History of the horizontal velocity component (e) and finite horizontal displacement (f) of tracers at 75 m depth located at radial distances from 10 to 18 km. The black lines delineate the arrival of the ejecta curtain.
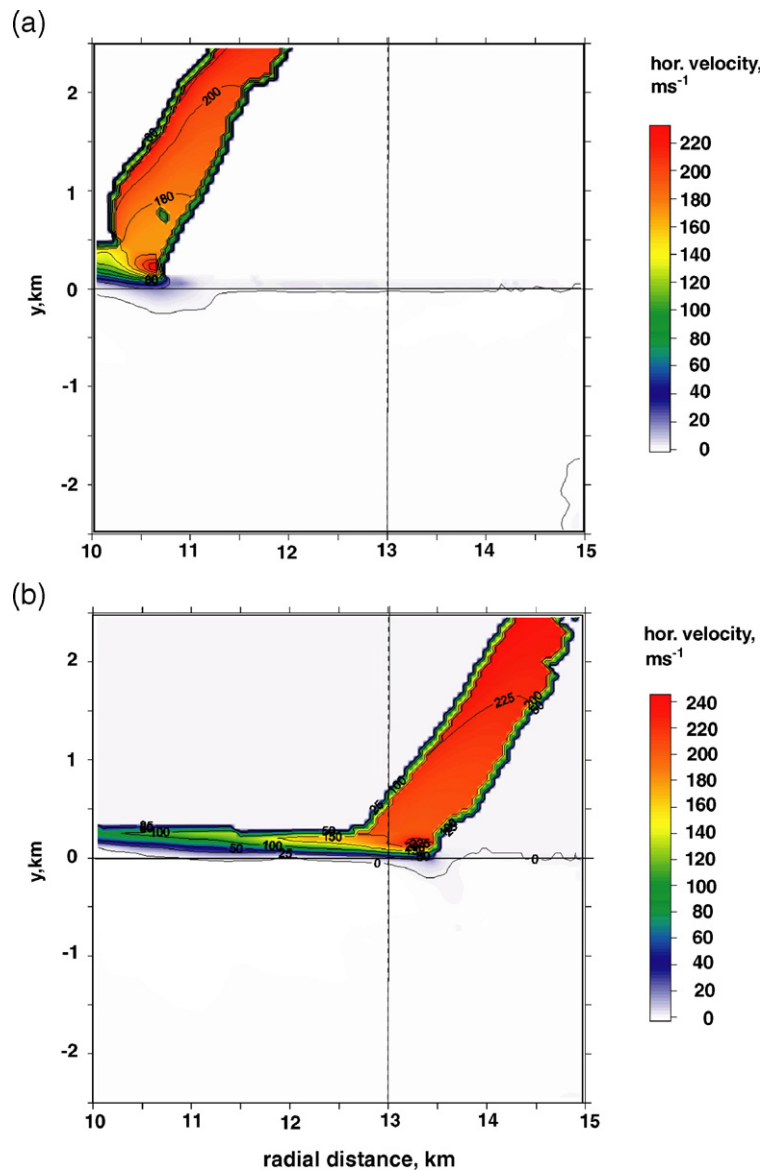
Fig. 7. Horizontal velocity distribution of the ejecta curtain and ejecta blanket in two time steps (∼ 40 s and 51 s, respectively), visualized by colour coding.

oblique trajectories of the ejecta curtain a horizontal momentum is delivered to the uppermost target area and results in a horizontal displacement increment by dragging. Ejecta dragging causes a distinct spike of 10–12 m/s that last for a few seconds. The dragging-induced horizontal displacement vanishes with depth and cannot be detected at a depth of 375 m and below (Fig. 6d). This trend in mind, it is straightforward to further focus on the uppermost tracers at 75 m depth for various crater distances: Fig. 6e illustrates the ejecta dragging effect for a radial distance ranging from 10 to 18 km. Amplitude and shape of the ejecta-induced velocity spikes change remarkably with

distance and become narrower. The non-uniform changes reflect the circumstance that ejecta deposited at the surface as lumps of material. Azimuthal variations, as expected, e.g., for oblique impacts or rayed ejecta would further influence the pattern in 3D models. The total amount of outward shearing of near-surface material is the sum of (i) spallation, (ii) the distant effect of transient cavity growth, and (iii) ejecta-induced dragging (Fig. 6f). It amounts to >1000 m at 10 km near the transient cavity rim and decays to ∼40 m at 18 km distance. Ejecta dragging adds a few decameters to total displacement budget (Fig. 6f).
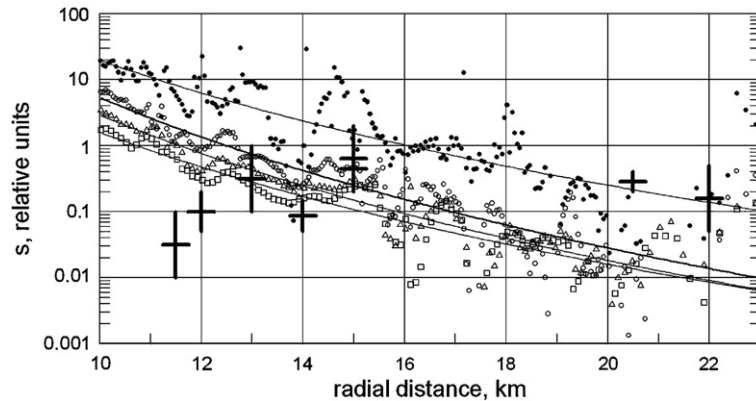
Fig. 8. Effective shear strain, *s*, vs. radial distance at a depth of 50 m (black circles), 100 m (open circles), 150 m (triangles) and 200 m (squares). As the upper subsurface cell row is disturbed by mixing with ejecta, these data show the largest noise. Data for effective shear strain follow a power-law decay with radial range (solid lines). Black crosses are field data recalculated for effective shear strain.

A comparison of shear strains recorded in the model and obtained by field observation is very crude, as no bulk strain could be measured directly in the field and was instead simply calculated by dividing the measured shear displacement by the depth of the shear plain. Fig. 8 shows the effective shear strain, *s*, with increasing radial distance as obtained from the model for various depths (50 m, 100 m, 150 m, 200 m). The effective shear strain decays both with depth and radial range from the center. The solid curves show power law trends for *s* at each depth (the exponent for the radial decay is around −7 for 10–20 km distances). Black crosses in Fig. 8 display our field data recalculated for effective shear strain. Note that field data only cover a range of 10–60 m depth and, thus, can only be compared with the model data for 50 m depth (black circles) (Fig. 8). According to the model, the shear deformation should be presented in most of upper sedimentary layers to depths of a few hundred meters at least. The model can, of course, not predict where and how shear localization occurs. From most field data effective shear strains are obtained with magnitudes in the range of *s* ∼ 0.1–1. A reasonably good agreement in *s* between field and model data is achieved for distances of 20–22 km from the crater center. The misfit increases to smaller distances.

5. Discussion and conclusion

We have observed several subhorizontal shear planes (detachments) in stratified target rocks at the crater rim and in the periphery of the Ries crater in Germany, and measured their displacement vector and magnitude. A systematic dependency seems to occur between the displacement and depth of these detachments and their distance with respect to the impact center. In combination with a numerical model we show that early spallation and subsequent dragging of the ejecta curtain are most likely responsible for the formation of detachments in the surrounding of the transient crater cavity. Modeling has shown that the effect of spallation followed by distant effects of transient cavity growth may dominate the effect of later dragging. This may, however, also depend on the spall strength of the material involved. Grady [30] determined a spall strength of 77 MPa for a Solnhofen limestone sample independent of impact amplitude, representing an upper strength level as rocks in natural state typically have a lot of fractures, decreasing the large scale strength. The effect of weak spallation in the periphery of the transient crater cavity can be enhanced by the layering of target material. Head and Melosh [31] demonstrated that a low-velocity layer of a thickness corresponding to the projectile radius can increase the spall velocity by steepening the near-surface pressure gradient. The rheological stratification of the Ries with a 700–800 m thick pile of sediments resting on a crystalline basement corresponds to the estimated projectile radius [8] and, thus, provides the prerequisite for effective spallation.

Modeling shows that spallation and ejecta dragging are two temporarily clearly distinct deformation increments with a hiatus of more than 30 s at one crater radius distance (final crater size). Since deformation features analyzed in the field always represent the sum of all deformation increments it is not easy to distinguish between both phases. However, it was possible to demonstrate that detachment faulting is the first crater related deformation increment. At the quarry Wemding (WEM), it could be demonstrated that radially outward directed motion did not come to rest when the gravity-driven collapse started. This indicates that ejecta curtain dragging played an important role for the total

displacement budget. The numerical model probably underrates the importance of the Bunte Breccia flow because it cannot accurately simulate the dynamics of the turbulent ejecta emplacement and complex ground motion that occur during ballistic sedimentation [20,16]. As the ejecta curtain expands over the target surface it entrains more and more locally derived surface material into a forceful radial outward flow. Near-surface delamination, detachment faulting, and hanging-wall dragging are precursor stages of the full incorporation of target material into the ejecta blanket. Moreover, the role of dragging of the ejecta could differ if atmospheric effects and impact obliquity are taken into account. Barnouin-Jha and Schultz [32] have shown that the geometry of the ejecta curtain is strongly affected by self-generated turbulent winds that can influence surface dragging.

The aim of the presented modeling was not to predict every detail observed in the field, but rather to determine the time sequence and extent of the major target motions (which are well modeled at the available resolution) and to provide boundary conditions for future, more detailed modeling work utilizing 3D numerical hydrocodes. The modeling is in some senses crude because of the low resolution of the mesh, and because some important physics were not implemented into the model, most significantly the effect of the fine-scale layering of the sedimentary target units, the effect of the atmosphere drag on ejecta emplacement, and an accurate description of the turbulent interaction of the ejecta with the target on which it lands. Note that in axial symmetrical 2D modeling each ejecta fragment represents a torus of material, while 3D ejecta may arrive as a stochastic cloud of ejected debris. A local 3D modeling is thus a prerequisite to refine theoretical predictions of a complex near-surface rock deformation.

We, therefore, emphasize that the model should not be over-interpreted. The modeling we used here to create a guideline for field data analysis is still very crude, as the cell-size is defined by a necessity to compute the entire cratering event to produce a proper loading pattern for stress waves and the depositing ejecta. The model is specifically designed to analyze the gross picture and time sequence of near-surface target deformation of a Ries-scale impact event. The presented low-resolution model may be used to construct boundary conditions for higher resolution models that focus on smaller areas. However, with the model accuracy available to date we can clearly state in accordance to field observations that for Ries-scale craters the upper ∼100 m of the target should be affected by the deposition of the ejecta curtain. Dragging near the target surface by the ejecta cause horizontal velocities of 5–50 m/s and displacements of a few deca-

meters at distances from 10 to 20 km from the Ries crater center. The pulse duration decreases with distance.

Near-surface decoupling of target material in the periphery of a crater may not occur uniquely at the Ries. It probably happened at the Lockne crater, Central Sweden [33] and is also recognized at Haughton Dome (Osinski, personal communication). The occurrence of subhorizontal dike systems in Cretaceaous target rocks of the Chicxulub crater (identified near the contact to suevitic ejecta at the Yaxcopoil drill site, 60 km distance from crater center) was interpreted as evidence for spallation decoupling [34]. Recently, lobe-parallel furrows and ridges structuring the inner portions of fluidized ejecta blankets of Martian impact craters, likewise require target detachments for their formation [5].

Acknowledgement

References

[1] H.J. Melosh, Impact cratering. A geologic process, Oxf. Monogr. Geol. Geophys. 11 (1989) (245 pp.).

[2] D.E. Maxwell, Simple Z model of cratering, ejection, and the overturned flap, in: D.J. Roddy, R.O. Pepin, R.B. Merill (Eds.), Impact and Explosion Cratering, Pergamon Press, New York, 1977, pp. 1003–1008.

[3] H.J. Melosh, Impact ejection, spallation, and the origin of meteorites, Icarus 59 (1984) 234–260.

[4] D.E. Grady, M.E. Kipp, The micromechanics of impact fracture of rock, Int. J. Rock Mech. Min. Sci. Geomech. Abstr. 16 (1979) 293–302.

[5] T. Kenkmann, F. Schönian, Ries and Chicxulub: impact craters on Earth provide insights for Martian ejecta blankets, Meteorit. Planet. Sci. 41 (2006).

[6] E.M. Shoemaker, E.C.T. Chao, New evidence for the impact origin of the Ries Basin, Bavaria, Germany, J. Geophys. Res. 66 (1961) 3371–3378.

[7] M.A. Laurenzi, G. Bigazzi, M.L. Balestrieri, V. Bouska, ^{40}Ar/^{39}Ar laser probe dating of the Central European tectite-producing impact event, Meteorit. Planet. Sci. 38 (2003) 887–893.

[8] J. Pohl, D. Stöffler, H. Gall, K. Ernstson, The Ries impact crater, in: D.J. Roddy, R.O. Pepin, R.B. Merill (Eds.), Impact and Explosion Cratering, Pergamon Press, New York, 1977, pp. 343–404.

[9] H.G. Kahle, Abschätzung der Störungsmasse im Nördlinger Ries, Z. Geophys. 35 (1969) 317–345.

[10] G. Angenheister, J. Pohl, Die seismischen Messungen im Ries von 1948–1969, Geol. Bavarica 61 (1969) 304–326.

[11] K. Ernstson, The structure of the Ries crater from geoelectric depth soundings, J. Geophys. 40 (1974) 639–659.

[12] K. Wünnemann, J.V. Morgan, H. Jödicke, Is Ries crater typical for ist size? An analysis based upon old and new geophysical data and numerical modeling, in: T. Kenkmann, F. Hörz, A. Deutsch (Eds.), Large Meteorite Impacts III, Geol. Soc. Amer. Special Paper, vol. 384, The Geological Society of America, Boulder, Colorado, 2005, pp. 67–83.

[13] D. Stöffler, Research drilling Nördlingen 1973 (Ries): Polymict breccias, crater basement, and cratering model of the Ries impact structure, Geol. Bavarica 75 (1977) 443–458.

[14] R. Hüttner, E. Brost, J. Homilius, H. Schmidt-Kaler, Struktur des Ries-Kraterrandes auf Grund geoelektrischer Tiefensondierungen, Geol. Jahrb. E19 (1980) 95–117.

[15] R. Hüttner, Zum Bau des südlichen Ries-Kraterrandes, Jahrb. Geol. Landesamt Baden Württemberg 30 (1988) 231–251.

[16] F. Hörz, R. Ostertag, D.A. Rainey, Bunte Breccia of the Ries: continuous deposits of large impact craters, Rev. Geophys. Space Phys. 21 (1983) 1667–1725.

[17] H.E. Newsom, G. Graup, D.A. Iseri, J.W. Geissman, K. Keil, The formation of the Ries crater, West Germany; evidence of atmospheric interactions during a larger cratering event, Geol. Soc. America Spec. Paper, vol. 247, The Geological Society of America, Boulder, Colorado, 1990, pp. 195–206.

[18] W.v. Engelhardt, Distribution, petrography, and shock metamorphism of the ejecta of the Ries crater in Germany—a review, Tectonophysics 171 (1990) 259–273.

[19] G.R. Osinski, R.A.F. Grieve, J.G. Spray, The nature of the groundmass of surficial suevite from the Ries impact structure, Germany, and constraints on its origin, Meteorit. Planet. Sci. 39 (2004) 1655–1683.

[20] V.R. Oberbeck, The role of ballistic erosion and sedimentation in lunar stratigraphy, Rev. Geophys. Space Phys. 13 (1975) 337–362.

[21] G.R. Osinski, Impact melt rocks from the Ries structure, Germany: an origin as impact melt flows? Earth Planet. Sci. Lett. 226 (2004) 529–543.

[22] G.H. Wagner, Kleintektonische Untersuchungen im Gebiet des Nördlinger Rieses, Geol. Jahrb. 81 (1964) 519–600.

[23] R. Hüttner, Bunte Trümmermassen und Suevit, Geol. Bavarica 61 (1969) 142–200.

[24] E. Seidl, Nördlinger Ries, eine typische Zerreiβ-Zone; entstanden durch tektonische Spannungen der Erdrinde, Z. Dtsch. Geol. Ges. 84 (1932) 18–23.

[25] H. Schmidt-Kaler, W. Treibs, R. Hüttner, Exkursionsführer zur Geologischen Übersichtskarte des Rieses 1:100,000, Bayerisches Geologisches Landesamt, München, 1970 (68 pp.).

[26] E.C.T. Chao, Impact cratering phenomenon for the Ries multiring structure based on constraints of geological, geophysical , and petrological studies and the nature of the impacting body, in: D.J. Roddy, R.O. Pepin, R.B. Merill (Eds.), Impact and Explosion Cratering, Pergamon Press, New York, 1977, pp. 405–424.

[27] D. Stöffler, N.A. Artemieva, E. Pierazzo, Modeling the Ries-Steinheim impact event and the formation of moldavite strewn field, Meteorit. Planet. Sci. 37 (2002) 1893–1907.

[28] G.S. Collins, H.J. Melosh, B.A. Ivanov, Modeling damage and deformation in impact simulations, Meteorit. Planet. Sci. 39 (2004) 217–231.

[29] T. Kenkmann, B.A. Ivanov, Thin-skin delamination of target rocks around the Ries crater: the effect of spallation and ejecta drag, Lunar Planet. Sci. Conf. 36 (2005) Cd-ROM #1039.

[30] D.E. Grady, Spall strength of Solnhofen limestone and Dresser basalt, Amer. Phys. Soc. Conf. Condensed Matter, Snowbird, 1999, abstract #P2.05.

[31] J.N. Head, H.J. Melosh, Effects of layering on spall velocity: numerical simulations, Lunar Planet. Sci. Conf. 30 (1999) Cd-ROM #1761.

[32] O.S. Barnouin-Jha, P.H. Schultz, Ejecta entrainment by impact-generated ring vortices: theory and experiment, J. Geophys. Res. 101 (1996) 21099–21115.

[33] E.F.F. Sturkell, J. Ormö, Impact-related clastic injections in the marine Ordovician Lockne impact structure, Central Sweden, Sedimentology 44 (1997) 793–804.

[34] T. Kenkmann, A. Wittmann, D. Scherler, Structure and impact indicators of the Cretaceous sequence of the ICDP drill core Yaxcopoil-1, Chicxulub impact crater, Mexico, Meteorit. Planet. Sci. 39 (2004) 1069–1088.